UNIVERSITY OF OKLAHOMA

GRADUATE COLLEGE

A MULTIDIMENSIONAL ANALYSIS OF AN ANOMALOUS, HIGH-IMPACT, EARLY-SEASON ICE STORM IN OKLAHOMA

A THESIS

SUBMITTED TO THE GRADUATE FACULTY

in partial fulfillment of the requirements for the

Degree of

MASTER OF SCIENCE IN METEOROLOGY

By

ALYSSA WOODWARD
Norman, Oklahoma
2022

A MULTIDIMENSIONAL ANALYSIS OF AN ANOMALOUS, HIGH-IMPACT, EARLY-SEASON ICE STORM IN OKLAHOMA

A THESIS APPROVED FOR THE
SCHOOL OF METEOROLOGY

BY THE COMMITTEE CONSISTING OF

Dr. Jeffrey B. Basara, Chair

Dr. Jason C. Furtado

Dr. Naoko Sakaeda

Acknowledgments

This work was supported by the National Science Foundation and Oklahoma EPSCoR under Grant No. OIA-1946093. I would first and foremost like to thank my advisor, Dr. Jeff Basara, for believing me and guiding me through each step in the research process. I would also like to thank my committee members, Dr. Jason Furtado and Dr. Naoko Sakaeda, for providing additional guidance that was beneficial to this study. Special thanks to Ollie Millin and Noah Brauer for their invaluable coding help and willingness to brainstorm ideas with me. Finally, none of this work would be complete without the unwavering support from my friends and family. There are not enough words to say thank you.

Contents

Abstract

Between 26 to 28 October 2020, an anomalous, high-impact, and early-season ice storm affected much of Oklahoma. This was the first time the National Weather Service (NWS) Forecast Offices in both Norman and Tulsa had issued an ice storm warning during the month of October and the event is the earliest ice storm in the last 40 years. Overall accumulations were consistent with past ice storm events, but the early season nature of this event led to higher impacts due to increased surface area for accumulations on trees that retained leaves from the growing season. This resulted in branch failures, many downed powerlines, and widespread power outages. Due to the early-timing and severe impacts the goal of this study is to investigate the evolution of the event and identify critical physical processes. First, the synoptic-scale and mesoscale features associated with the event were examined. At the synoptic-scale, a 500 hPa Alaskan ridge, ample 700 hPa moisture transport from the eastern Pacific Ocean region, and the progression of cold 850 hPa temperature anomalies from Canada were all noted 14 days before ice storm onset. At the mesoscale, deep-tropospheric ascent contributed to the significant, localized heavy precipitation across central Oklahoma that was collocated with an anomalous, shallow cold air mass. Second, the October 2020 ice storm was compared to 12 past ice storms in Oklahoma that occurred between 1996 and 2017 to investigate whether the synoptic-scale patterns of an early-season storm differ from normal winter season events. The results yielded similar overall patterns, however, the magnitude of anomalies was generally greater for October 2020 than other past cases. Finally, a potential predictability signal was identified where the geopotential height pattern of past ice storms exists simultaneously with cold 2-meter temperature anomalies over much of the CONUS spanning up to two weeks before event onset.

1. Introduction

Ice storms, which the National Weather Service (NWS) defines as freezing rain accumulations over 0.635 cm (0.25 inch) (Degalia et al. 2016), are high-impact events that yield crippling impacts across space and time (Andrei et al. 2019, Bendel and Paton 1982, Call 2009, Call 2010, Changnon 2003a, Changnon and Karl 2003, Degalia et al. 2016, Grout et al. 2012, Mullens et al. 2016, Ramos Da Silva et al. 2006, Rauber et al. 1994, Roebber and Gyakum 2003). Freezing precipitation and ice pellets occur most often in the boreal winter months (December through March) in the United States (US) and Canada (Cortinas Jr. et al. 2004). More specifically, they are the most common in December for northwest Oklahoma and in January for central and southern Oklahoma (Changnon and Karl 2003). In the case of ice storms, three main ingredients are critical including a shallow layer of subfreezing air near the surface (Bendel and Paton 1982). Second, a deep, warm layer in the mid-levels, also known as a "warm nose" on a sounding is important as it will allow any frozen precipitation to melt thereby forming droplets which become supercooled in the cold layer near the surface. If the temperature is below freezing, any exposed surfaces will accumulate ice. A third ingredient is a source of dynamic ascent which usually occurs at the synoptic-scale when a warm, humid air mass surges over a cold air mass, whose origin is continental polar (Bendel and Paton 1982). Even so, significant variability exists in favorable synoptic-scale patterns across different regions in the US (Robbins and Cortinas, 2002). For example, ice storms have been shown to occur in association with 1) an arctic front and anticyclone, 2) a warm front or occlusion sector of a cyclone, 3) cyclone and anticyclone interactions, and 4) the western quadrant of an arctic high. Rauber et al. (2001) and Mullens et al. (2016) noted that ice storms in the United States are most frequently caused by Arctic cold fronts moving southward as warm, moist air ascends over the front. Mullens et al.

(2016) further noted that high impact ice storms in the Southern Great Plains (SGP) are associated with slow-moving upper-level flow, persistent isentropic ascent over a quasi-stationary front with strongly positive moisture anomalies, and warm layer air mass trajectories that originate over the Gulf of Mexico. Large-scale climate patterns such as the El Niño-Southern Oscillation (ENSO), Madden-Julian Oscillation (MJO), and North Atlantic Oscillation (NAO) can enhance or suppress favorable environments for winter weather. Generally speaking, La Niña leads to drier and warmer conditions while El Niño leads to wetter conditions across the southern US in the winter months (Ropelewski and Halpert 1986). The MJO can result in an increase in the frequency and intensity of cold air outbreaks in the eastern US. Finally, the negative phase of the NAO is associated with stronger cold air outbreaks and increased storminess in eastern North America whereas the positive phase is associated with suppressed conditions (Cassou 2008).

The economic and social costs from high-impact ice storms are compounded due to 1) the infrequent nature of freezing rain events and 2) fewer resources to treat the excessive ice as it accumulates on exposed surfaces, including roads, power lines, and utilities (Grout et al. 2012). At the same time, of all winter weather events, ice storms produce the greatest frequency of disaster conditions (Grout et al. 2012). Ice storms can be very costly, averaging in excess of $300 million per year in the United States (Zarnani et al. 2012). However, geographic variations are significant (Changnon 2003a). Across the Southern Climate Region, from 1949 to 2000 ice storm catastrophes yielded $2.184 billion (Changnon 2003a) in costs. Further, the National Centers for Environmental Information (NCEI) Storm Events Database reported that from 1996 to 2012 a total of 95 deaths and 331 injuries were directly caused by ice storms in the US with an average of 5.59 and 19.47 reports per year respectively. Power outages during ice storms are the

most adverse and direct impact to households because people have no way to heat their home (Call 2010). Such power outages are driven by ice accumulations which can increase the branch weight by up to 30 times its original weight (Hauer et al. 1993) resulting in branch failure. Further, accumulations of 0.635 to 1.27 cm (0.25 to 0.5 in) can cause small branch failures whereas 1.27 to 2.54 cm (0.5 to 1 in) can cause serious breakage and even damage healthy young trees. Other major impacts of ice storms include transportation disruptions, shutdown of commercial businesses, and agricultural losses (Grout et al. 2012; Rauber et al. 2001; Ressler et al. 2012).

Although ice storms in Oklahoma are less frequent than snowstorms they do still occur. From 1949 to 2000 the entire state of Oklahoma experienced 11 catastrophic ice storms or approximately two per decade (Call 2009). The frequency of ice storms is increasing especially in the past few decades (Changnon and Karl 2003). From 2000 to 2010 seven individual counties within Oklahoma experienced four or more catastrophic ice storms (Grout et al. 2012). Twelve notable ice storms have specifically impacted Oklahoma since 1996 and are included in the analysis of this study. Specific examples include:

- On December 26, 2000 an ice storm occurred across Arkansas, Oklahoma, Texas, and Louisiana. Specifically in Oklahoma, nearly an inch of ice accumulated resulting in 26 deaths, 170,000 without power at its peak, and $200 million in state and federal aid required to mitigate the impacts. Freezing rain fell for three consecutive days prompting Gov. Franking Keating to declare all 77 Oklahoma counties federal disaster areas (National Weather Service 2001).
- On January 30, 2002 across north and west-central Oklahoma an ice storm event resulted in seven fatalities, $100 million in damage, and 125,000 cubic yards of

tree debris in Oklahoma City alone. Most areas received an inch or more of ice accumulation with a west to north-central corridor receiving a six-inch thick frozen layer. At the storm's peak, more than 255,000 residents were without power and the Oklahoma Association of Electric Cooperatives reported 31,000 electrical poles destroyed due to ice. Electric power was not fully restored to all Oklahoma City residents until 11 days after the storm and to all Oklahoma residents until months later. Due to the impacts of the event, 45 Oklahoma counties were declared federal disaster areas (Oklahoma Mesonet 2002).

- An ice storm occurred on December 9, 2007 whereby over an inch of ice accumulated across the majority of Oklahoma. The event resulted in 27 deaths, primarily from automobile accidents, and Gov. Brad Henry issued a State of Emergency for all 77 Oklahoma counties. During the peak of the event, 641,000 Oklahoma residents were without power due to the storm. At the time, this was the worst power outage in Oklahoma history in terms of the number of people impacted. One week after the storm 150,000 residents were still without power. Storm cleanup was estimated at $200 million and cities removed over 750,000 cubic yards of debris (National Weather Service 2008).
- The ice storm event that occurred on December 27, 2015 yielded a swath of ice accumulations ranging from 0.25 to 1 inches. This was a multi-hazard event with snow, ice, and tornadoes impacting most of the Great Plains and Midwest. The ice that fell in Oklahoma was accompanied by high winds gusting to more than 70 mph and localized flooding in eastern Oklahoma. The event resulted in 200,000 residents without power and 955 traffic collisions (Mesonet 2016).

This study examines a historic and anomalous ice storm that impacted the majority of the state of Oklahoma from 26 to 28 October 2020 which included the distinction that it was the first time the NWS Forecast offices in both Norman and Tulsa issued an ice storm warning in the month of October. Due to the anomalous nature of this event specifically and the impact all ice storms can have on society the following research questions will be addressed as part of this study (i) What were the critical physical drivers of the October 2020 ice storm and how did they evolve? (ii) How does this "early-season" ice storm compare to past ice storm events? (iii) Do predictability features exist that could be used to improve forecasting of ice storm events?

2. Data and Methods

2.1 Data

2.1.1 ERA-5

This study used the European Centre for Medium Range Weather Forecasts (ECMWF) Reanalysis Fifth Generation (ERA-5) dataset (Hersbach et al. 2020). For the period spanning September to January (SONDJ) 1979 to 2020 and specifically October 2020, the hourly dataset comprised a 0.25° horizontal resolution on a regular longitude-latitude Cartesian grid with 37 vertical levels from 1000 hPa to 1 hPa. The following variables were used: geopotential, specific humidity, temperature, and the horizontal and vertical components of the wind across a spatial domain of 30°S to 80°N and 125°E to 10°W.

2.1.2 GridRad

This study also used GridRad horizontal radar reflectivity factor (Bowman and Homeyer 2017) derived from NEXRAD WSR-88D data. The temporal resolution from 26 October 2020 at 0000 UTC to 29 October 2020 at 0000 UTC spanned every 5 minutes at a 0.02° horizontal resolution and a 0.5 km vertical resolution below an altitude of 7 km, and 1 km vertical resolution between an altitude of 7 to 22 km. The longitude-latitude-altitude Cartesian grid covered a spatial domain of 31° to 41°N and 104° to 90°W.

2.1.3 NCEI Storm Events Database

A dataset of past ice storm events from November 1996 to January 2017 was compiled using the National Oceanic and Atmospheric Administration (NOAA) National Centers for Environmental Information (NCEI) Storm Events Database (https://www.ncdc.noaa.gov/stormevents/). This database archives notable weather events by county, state, start date and time, and weather type with a brief overview of each event. Twelve

past ice storm events were identified for Oklahoma and were used for analysis in this study. They are listed in Table 1.

Table 1. List of past ice storm start dates that affected Oklahoma.

Event	Date
1	11/24/96
2	12/21/98
3	1/7/99
4	12/26/00
5	1/30/02
6	12/3/02
7	12/9/07
8	1/28/10
9	12/20/13
10	11/27/15
11	12/27/15
12	1/13/17

2.1.4 Additional Data

Datasets of the ENSO, MJO, and NAO phases were used in this study. ENSO phases of the 12 past ice storm cases are obtained from the National Centers for Environmental Prediction (NCEP) Climate Prediction Center (CPC) (https://origin.cpc.ncep.noaa.gov/products/analysis_monitoring/ensostuff/ONI_v5.php). The CPC uses the Oceanic Niño Index (ONI) based on a threshold of +/- 0.5°C calculated with a three-month running mean of NOAA's Extended Reconstructed Sea Surface Temperature Version 5 (ERSST.v5) SST anomalies in Niño 3.4 region (5°S to 5°N and 170° to 120°W) based on 30 year base periods updated every five years. The MJO phases were obtained from the Australian Government Bureau of Meteorology

(http://www.bom.gov.au/climate/mjo/#tabs=MJO-phase) that are identified by their locations along the equator around the globe using the Real-Time MJO Monitoring Index (Wheeler and Hendon 2004). The NAO phases were obtained from the NCEI (https://www.ncdc.noaa.gov/teleconnections/nao/). The NAO index is calculated by projecting the NAO leading pattern to the 500 hPa geopotential height daily anomaly field over 0° to 90°N. The NAO leading pattern is the first mode of a rotated Empirical Orthogonal Function (EOF) analysis using monthly mean 500 hPa geopotential height anomalies from 1950 to 2000 over 0° to 90°N.

2.2 Methods

2.2.1 GridRad Viewer

GridRad-Viewer is an interactive application for visualizing high-resolution three-dimensional GridRad data. It was developed in Interactive Data Language (IDL) by Dr. Cameron Homeyer. This study used GridRad-Viewer to analyze horizontal radar reflectivity factor from 26 to 29 October 2020.

2.2.2 ERA-5 Reanalysis

Many types of analyses were completed using ERA-5 reanalysis data. First, isentropic ascent was analyzed for the period spanning 24 to 26 October 2020 to examine a possible source of lower- to mid-level lift necessary for extreme precipitation. If an adiabatic process is assumed, isentropic ascent is pressure advection along constant potential temperature surfaces, or isentropes (Namias 1938). During ascent, air parcels will move from areas of higher pressure to areas of lower pressure and is analogous to warm temperature advection on constant pressure surfaces. For this analysis the Metpy Calculations (metpy.calc) package called 'isentropic_interpolation' was utilized and required the following input variables: isentropic

level, pressure levels (1000 hPa to 1 hPa), temperature, u-, and v-components of the wind, specific humidity, and geopotential height (May et al. 2022). Vertical linear interpolation was used to calculate pressure at each isentropic level. It was also assumed that temperature varies linearly with the natural log of pressure and all other variables vary linearly with temperature.

To investigate ascent at all levels of the atmosphere, vertical cross sections of potential temperature and the w-component of wind from 24 to 26 October 2020 were plotted along the 97.5°W longitude line from 20°N to 50°N and 1000 hPa to 1 hPa.

To isolate the analysis of ascent to only the upper tropospheric conditions, u- and v-components of the wind and lines of constant geopotential height contours were plotted at 250 hPa from 24 to 26 October 2020. Wind barbs are obtained from the components of the wind and shading is added starting at 75 knots and every 25 knots after.

Spatial maps of 500 hPa geopotential height, 700 hPa specific humidity, and 850 hPa temperatures anomalies using a daily climatology (SONDJ 1979 to 2020) for lag day 14, 10, 7, 4, 2, and 1 before event onset of the October 2020 ice storm were created.

The sea surface temperature (SST) and 250 hPa quasi-geostrophic (QG) streamfunction anomalies were computed using a daily climatology (SONDJ 1979 to 2020) and streamfunction was averaged for the period spanning September - November (SON) 2020 and for October 2020. The QG streamfunction was calculated by dividing the Coriolis parameter from geopotential for every grid point as seen in the following Eq. 1.

$$\psi = \frac{\phi}{f} \tag{1}$$

where ϕ is geopotential and f is the Coriolis parameter. QG streamfunction is analogous to geopotential height except it accounts for a latitude correction. It should be noted that streamfunction was not plotted from 10°S to 10°N as QG Theory is not applicable in the tropics.

To compare the October 2020 ice storm to past events, time-lagged composites of 500 hPa geopotential height, 700 hPa specific humidity, and 850 hPa temperature anomalies are created. For each atmospheric variable, anomalies for each past ice storm were calculated using a daily climatology (SONDJ 1979 to 2020) and averaged to obtain spatial analyses. This was completed for lag day 14, 10, 7, 4, 2, and 1 before event onset. Finally, 5000-iteration bootstrapping without replacement was performed to determine statistical significance at the 95th percentile. The advantages to utilizing bootstrapping include (1) the dataset is less sensitive to sample size, compared to t-testing and (2) an underlying distribution is not assumed.

To further compare the October 2020 ice storm to past events, bar charts of each events' (including October 2020) 500 hPa geopotential height, 700 hPa specific humidity, and 850 hPa temperature anomaly minimums and maximums were created for lag day 1. This was completed because the magnitudes of the time-lagged composites will be less than the magnitudes of just the October 2020 event based on the nature of averaging the 12 past ice storm cases. Therefore, decomposing each individual event is necessary.

An analysis was completed to investigate if the October 2020 850 hPa temperature field still showed anomalous features if it were to occur in December or January, which are months most common for ice storms in Oklahoma, rather than October. Therefore, instead of using a daily climatology to calculate anomalies, the end of December and January periods (days 15 through 31) of 1979 to 2020 average 850 hPa temperature were subtracted from 26 - 28 October 2020 average.

To identify a predictability feature matrix multiplication (i.e. the dot product of the lag day 14 and lag day 1 composites, standardized geopotential height anomalies and the standardized geopotential height anomalies for each day (SONDJ 1979 - 2020) in the dataset)

was completed. This created a time series of standardized indices for each day measuring how well a particular day matched the lag day 14 and lag day 1 composites. As part of the analysis, a positive index yields a match where the higher the magnitude the more it aligns. Conversely, a negative index means they have a similar pattern to the composite but with an opposite sign. Any day whose index exceeded two was composited and the averaged 500 hPa geopotential height anomalies were projected onto a map. Finally, using the same days that encompassed the geopotential height maps, standardized 2 meter temperature anomalies were composited. This displayed surface temperature conditions for days whose geopotential height pattern matched the lag day 14 and lag day 1 composites.

2.2.3 Teleconnections

A box and whisker plot was created to visualize what ENSO, MJO, and NAO phases the 12 past ice storms and the October 2020 ice storm were in during event onset. It consisted of the minimum value, second quartile (lower 25% of the data), median value, third quartile (upper 25% of the data), and maximum value. ENSO is a reoccurring climate pattern involving the changes in SSTs in the central and eastern tropical Pacific Ocean. This irregular variation in SSTs directly affects rainfall distribution in the tropics and has a strong influence on weather across the United States (Ropelewski and Halpert 1986). The MJO is an eastward moving disturbance of clouds, rainfall, winds, and pressure that traverses along the equator and returns to its initial starting point on average every 30 to 60 days. MJO-related effects on the Indian and West African summer monsoon are well documented, however, connections to North American winter precipitation have recently been investigated (Schwartz and Garfinkel 2017). The NAO index describes the changes in the relative strength of two recurring pressure patterns in the North Atlantic Ocean: the subpolar low and subtropical high. A positive index indicates the

subpolar low and subtropical high are stronger than normal leading to a more dynamic Atlantic jet stream. Whereas a negative index indicates the subpolar low and subtropical high are weaker than normal leading to a more east-west oriented Atlantic jet stream (Lamb and Peppler 1987).

3. Results

3.1 26 to 28 October 2020 Event Summary

3.1.1 Overview

At the synoptic scale a 500 hPa southwest-northeast oriented, positively tilted, longwave trough was positioned from northeast Montana to central California on 25 October at 0000 UTC. It continued to deepen and eventually transitioned to a 5520 m closed low by October 27 at 1200 UTC over southern Arizona. This brought upper-level southwesterly flow to central Oklahoma. It then moved to the northeast through Oklahoma before interacting with Hurricane Zeta on 29 October. At the surface a 9980 m surface low centered over southwestern Colorado on 25 October at 0000 UTC rapidly moved south to southern New Mexico by 27 October at 0000 UTC. A broad stationary front extending to a cold front from the surface low to the east coast of Texas brought northerly to northeasterly surface flow to central Oklahoma throughout the entirety of the event before also interacting with Hurricane Zeta on 29 October 0000 UTC. From 27 October at 0000 UTC to 28 October at 0000 UTC a surface high was centered in central Kansas.

Greater than an inch of ice accumulated across Oklahoma with the greatest accumulations to the northwest and west of the Oklahoma City metro. Because most deciduous trees had not shed their leaves, the result yielded increased surface area for ice accumulation. As such, the increased weight led to tree branches that snapped which contributed to many downed power lines. This was unique to this event as it was the earliest ice storm in the past 40 years. At the peak, over 400,000 customers in Oklahoma were without power and OG&E reported the single largest storm-related outage in its history. There were 132 injuries as a result of this storm (OK Mesonet). On 26 October Gov. Kevin Stitt had issued an Emergency Declaration for 47 counties

in Oklahoma (FEMA). FEMA announced on December 21 a Major Disaster Declaration for 13 counties in Oklahoma estimating $27 million in debris removal and other damages. The Oklahoma Mesonet said this storm was “arguably the most impactful early-season winter storm in the history of Oklahoma.”

3.1.2 Radar Reflectivity

The October 2020 ice storm included three intervals of ice-accumulating, stratiform precipitation over the course of three days ranging from 10 to 50 dBZ (Fig. 1). The first round of precipitation arrived in central Oklahoma from the southwest at approximately 0900 UTC on 26 October and ice accumulation was nearly continuous in central Oklahoma through 0000 UTC on 27 October. Then, most of the precipitation moved out of Oklahoma but there was lighter precipitation in southeastern Oklahoma and the Panhandle in the overnight hours of 27 October. The second wave of accumulating ice arrived in central Oklahoma at approximately 1100 UTC on 27 October. Heavier precipitation which subsequently lasted for six hours with much lighter precipitation through 0000 UTC on 28 October that moved off to the north and northeast. The third round began at approximately 0700 UTC on 28 October with lighter precipitation moving in from Texas. Moderately heavy precipitation lasted until approximately 2100 UTC on 28 October in central Oklahoma.

3.1.3 Low-level, Mid-level, and Upper-level Ascent

To understand the drivers of the precipitation intervals, ascent through the troposphere was examined at various levels. Via the 304 K isentropic analysis in Figure 2, at 0600 UTC on 26 October isentropic ascent was strong in the lower-levels as the southerly wind barbs were mostly perpendicular to the isobars across Texas and Oklahoma. As such a moist air mass with specific humidity values near 16 g/kg was rising from approximately 900 hPa through 725 hPa

with a fetch that originated off the west coast of Mexico south of Baja California Sur in the Pacific Ocean. Moisture contributions from the Gulf of Mexico appeared to be minimal on 26 October.

Vertical motion in the low- to mid-levels of the atmosphere was the highest at 1500 UTC on 26 October (Fig. 3). The vertical motion reached a maximum of approximately 2 Pa s^{-1} from 700 hPa through 300 hPa over the latitude of Oklahoma City (~35.5°N) contributing to a broad region of strong mid-level ascent. At the same time, the isentropes sloped upward from 1000 hPa to 700 hPa over a shallow layer of cold air from 25°N to 45°N and due to a frontal boundary. Overall, this led to continuous, modest vertical motion from the surface to the mid-troposphere allowing for heavy precipitation to occur.

During the October 2020 ice storm a jet streak was located in the Great Lakes region which put Oklahoma in the right entrance region which is an area of upper-level divergence that leads to ascent. A second jet streak was located in the northwest US and upstream of the positively tilted upper-level trough axis that spanned the majority of the contiguous US. The placement of this jet streak allowed the trough to dig and remain relatively stationary during the ice storm. As such, Oklahoma was located downstream of this trough axis which is where synoptic-scale ascent occurred. Further, the upper-level ascent steadily increased through the event and peaked at 1800 UTC on 26 October via divergence aloft in the right entrance of a jet streak displayed via the 250 hPa analysis in Figure 4.

The thermodynamic profile from October 2020 in Figure 5 showed a pronounced “warm nose” in the mid-levels, especially on 28 October, above a shallow, cold layer near the surface. This was reflected in the wind profile with primarily southwesterly winds at the levels with a “warm nose” and primarily northeasterly winds at the levels with a shallow, cold layer. Another

important feature on the soundings was the gradual moistening of the column. On 26 October the thermodynamic profile was saturated to 800 hPa and on 27 and 28 October to 650 hPa. This is a function of the deep-tropospheric ascent that occurred during this event.

3.1.4 Synoptic Evolution

To determine the evolution of the atmospheric conditions that contributed to the event, analyses of 500 hPa geopotential height, 700 hPa specific humidity, and 850 hPa temperature anomalies as far back as two weeks before event onset were examined.

At 500 hPa in Figure 6, geopotential height anomalies on lag day 14 displayed higher anomalies over the Kamchatka Peninsula, central Canada, the Great Lakes region, and southeast of Greenland and lower anomalies over the Aleutian Islands, western Canada, the high plains of the US, and far eastern Canada. By lag day 10 this pattern shifted eastward such that higher anomalies existed over Alaska, the West Coast of the US and British Columbia, and the East Coast of the US and lower anomalies existed over central Canada and the US. This pattern strengthened with time, especially the Alaskan Ridge and low pressure southeast of Greenland. By lag day 2, a notable Rossby wave train extending from eastern Asia to the north central Atlantic Ocean developed and this dynamic upper air pattern remained consistent through lag day 1.

The analyses of specific humidity anomalies at 700 hPa in Figure 7 revealed a pattern that did not evolve with time but rather showed consistent, stationary signals. Throughout each lag day, channels of higher water vapor anomalies, that originated in the tropics, extended northward to the contiguous US and were reflective of atmospheric rivers. These channels were especially prominent through the central Pacific Ocean and Caribbean on lag day 2 and lag day 1.

For 850 hPa temperature anomalies in Figure 8, on lag day 14 no clear patterns were present. However, on lag day 10, cold air from the Arctic extended into central Canada and the US while warm anomalies appeared off both the West Coast and East Coast of the US. This pattern of a cold, polar air mass in the central US wedged between two warmer air masses off both coasts of the US remained persistent through lag day 1. At the same time, the anomalous nature of the cold air mass became even colder with time in central Canada and the US.

3.1.5 Sea Surface Temperature and Streamfunction Anomalies

To aid in understanding the role of teleconnections on the event, SST and 250 hPa QG streamfunction anomalies up to two months before event onset were examined. Cold SST anomalies were prevalent across the central and eastern tropical Pacific Ocean indicative of a pronounced La Niña period for both SON 2020 (Fig. 9a) and October 2020 (Fig. 9b).

When the SST and 250 hPa QG streamfunction anomalies were compared for October 2020, positive streamfunction anomalies (higher heights) were collocated with warmer SSTs east of Japan, off the West Coast of the US and British Columbia, and off the East Coast of the US. Conversely, negative streamfunction anomalies, or lower heights, were collocated with colder SSTs over the central Pacific Ocean.

3.2 Climatological Analysis of the October 2020 Ice Storm

3.2.1 Time-lagged Composites

To expand the synoptic analysis of the October 2020 ice storm and compare with other known events for the region, time-lagged composites were examined to identify patterns in the 500 hPa geopotential height, 700 hPa specific humidity, and 850 hPa temperature anomalies for a period spanning two weeks before event onset. The historical cases are noted in Table 1.

At 500 hPa in Figure 10, the composite geopotential height anomalies on lag day 14 include higher anomalies over the Aleutian Islands, far eastern Canada, and along the East Coast of the US and lower anomalies over the Kamchatka Peninsula, central Canada and the US, and Greenland. Further, the only notable statistically significant 500 hPa height anomalies were identified over the Kamchatka Peninsula and southeastern US locations. By lag day 10 higher anomalies were located from Alaska south along the west coast of Canada and the US and the East Coast of the US and lower anomalies over central Canada and the US and south of Greenland. Further, the spatial regions of statistical significance increased and expanded significantly. Overall, the mid-tropospheric pattern remained relatively stationary through lag day 1 with slight eastward and westward shifts in the local minima and maxima of geopotential height anomalies. An area of statistically significant, lower geopotential height anomalies was also located southeast of Greenland and were present from lag day 10 through lag day 4 before translating eastward out of the spatial domain of this study on lag day 2. More importantly, the Alaskan Ridge became a statistically significant feature on lag day 4 which broadened and increased in magnitude through lag day 1 while the downstream trough over central Canada and the US became statistically significant on lag day 2. This trough region also broadened and increased in magnitudes through lag day 1. Finally, on lag day 1 there were regions of statistically significant higher anomalies over the south-central US and off the East Coast of the US.

For the 850 hPa temperature anomalies in Figure 11, the most noticeable signal through each lag day was the -12ºC cold anomaly over central Canada and the US. On lag day 14 the composite pattern displayed statistical significance in the central plains and western US. The composite cold anomaly remained present with minor shifts northward and eastward through lag

day 4 and on lag day 2 the magnitude of the composite cold anomaly dramatically increased and a broad region of statistical significance developed over much of Canada. By lag day 1, the magnitude of the composite cold anomaly and the region of broad statistical significance further increased with expanded statistically significant regions including the SGP of the US and over the Aleutian Islands. Next, the 850 hPa temperature field for October 2020 was compared to the end of December (Fig. 12a) and end of January (Fig. 12b) averages, instead of a daily climatology. The majority of the domain consisted of positive anomalies which is to be expected as the climatology of October 850 hPa temperatures should be warmer than December and January in the midlatitudes. A more notable feature using both December and January averages was the cold anomaly in the central US.

At 700 hPa in Figure 13, the anomalies of specific humidity displayed no clear, consistent patterns or regions of statistical significance through each lag day. This is likely due to the fact that anomalies of specific humidity occur on smaller spatial and temporal scales than anomalies of 500 hPa geopotential height and 850 hPa temperature and ERA-5 is too coarse to capture the variability.

As an extension of the time-lagged composites, the minimum and maximum 500 hPa geopotential height, 700 hPa specific humidity, and 850 hPa temperature anomalies for each of the 12 past events and October 2020 for lag day 1 are presented in Figure 14. Overall, the October 2020 ice storm had the fifth highest 500 hPa geopotential height anomaly maximum (+375 m) within the Alaskan Ridge (Fig. 14a) and the fourth lowest 500 hPa geopotential height anomaly minimum (-350 m) within the trough southeast of Greenland (Fig. 14b). Additionally, the 2020 event had the highest 700 hPa specific humidity anomaly maximum (+9 g/kg) off the East Coast of the US (Fig. 14c) while the 12 past cases yielded anomalies of approximately 6

g/kg. The 2020 event also had the lowest 700 hPa specific humidity anomaly minimum (-5 g/kg) south of Japan (Fig. 14d) while the 12 past cases yielded anomalies of approximately -3.5 g/kg. Finally, the October 2020 ice storm had the third warmest 850 hPa temperature anomaly maximum (+14 °C) that occurred south of the Aleutian Islands associated with the Alaskan Ridge (Fig. 14e) along with the third coldest 850 hPa temperature anomaly minimum (-23 °C) that occurred in the northwest US (Fig. 14f).

3.2.2 Teleconnections

Ice storms in Oklahoma are associated with different phases of large-scale climate patterns where identifying these phases may increase the understanding of them as they occur on the subseasonal to seasonal (S2S) time scale. The phases for the ENSO, MJO, and NAO are presented in a box and whisker plot in Figure 15. Ice storms can occur during the positive or negative phase of ENSO. However, they tend to hinge toward La Niña periods as seen by the median value. The October 2020 event occurred during a La Niña period as well. The polar jet stream during La Niña tends to result in the Alaskan Ridge and downstream trough which is conducive to polar air transport and favorable for ice storm formation. Ice storms can occur during phases 4 to 7 of the MJO however phases 6 and 7 are the most common. During the October 2020 event the MJO transitioned from phase 6 on 27 October to phase 7 on 28 October. Similar to ENSO, ice storms can occur during the positive and negative phase of the NAO. They tend to hinge more toward the positive phase as seen by the median value; however, during the October 2020 event the NAO was in a relatively strong negative phase.

3.3 Identification of a Predictability Feature

Every day in the dataset (SONDJ 1979-2020) was compared to the lag day 14 and lag day 1 500 hPa geopotential height composites to investigate whether a reoccurring pattern appeared

that is conducive to ice storms. When the dot product was applied, the time series for both lag day 14 (Fig. 16a) and lag day 1 (Fig. 17a) revealed a relatively stationary distribution about the zero index. Lag day 14 had 150 days that exceeded an index of two and lag day 1 had 208 days that exceeded an index of two.

These days were composited and 500 hPa standardized geopotential height anomalies were projected onto a map. Lag day 14 (Fig. 16b) revealed a "wave train" with higher anomalies over Alaska, western Canada, and from the Gulf of Mexico north along the East Coast of the US to eastern Canada and lower anomalies over the Kamchatka Peninsula, central Canada, the western half of the US, and southeast of Greenland. By lag day 1 (Fig. 17b) the "wave train" subsided and became less dynamic. However, two distinct features became more prominent from lag day 14: the Alaskan Ridge, which expanded to the southwest, and the downstream trough centered over the US-Canada border.

The same days that were composited for the 500 hPa geopotential height analysis were also used to project 2 meter standardized temperature anomalies onto a map. The lag day 14 (Fig. 16c) and lag day 1 (Fig. 17c) maps had a very similar pattern. A warm anomaly extended from the Arctic south through eastern Siberia and Alaska. To the east, a cold anomaly extended down from northwestern Canada south through the western and central US. Finally, a warm anomaly occurred over the eastern US and Gulf of Mexico. The difference is during lag day 1 the cold anomaly extended farther east in the contiguous US which shifted the warm anomaly off the East Coast of the US and the magnitude of the anomaly lowered.

4. Discussion

Many features of the October 2020 ice storm were consistent with past events. However, this study revealed new insights into the processes that made this event so impactful in October. The first and most important pattern involved the presence of the Alaskan Ridge and downstream trough (i.e. via the 500 hPa composite analyses). This pattern developed on lag day 10 prior to the onset of the October 2020 event and lag day 14 for the time-lagged composites. Recently, Millin et al. (2022) demonstrated that the Alaskan Ridge is a critical feature associated with cold air outbreaks in the Great Plains. In October 2020 this pattern allowed anomalously cold air to extend from the Arctic to the SGP. Further, while the upper air pattern was similar to past ice storm events, the magnitudes of the anomalies for the October 2020 case when compared to other past events yielded the fifth highest 500 hPa geopotential height anomaly maximum (+375 m) and the fourth lowest 500 hPa geopotential height anomaly minimum (-350 m) on lag day 1.

Another feature present in the composites was the 850 hPa cold anomaly in central Canada and the US which developed on lag day 14 with statistical significance for the time-lagged composites and lag day 10 for October 2020. Again, as noted by Millin et al. (2022), the upper air geopotential height pattern, specifically the Alaskan Ridge, is critical to the development of this feature. Also similar to the 500 hPa geopotential height anomalies, the magnitudes of the temperature anomalies for October 2020 were high compared to previous events. From lag day 14 through lag day 4 the composite average cold anomaly was analyzed at approximately -3°C whereas the magnitude for October 2020 from lag day 10 through lag day 4 was approximately -10°C. As such, October 2020 had the third lowest 850 hPa temperature anomaly minimum (-23°C) on lag day 1 whereas the average anomaly minimum for the 12 past ice storms was near -17°C. Because the October 2020 ice storm happened so early in the winter

season, the magnitude of the cold anomalies needed to be high to produce a winter weather event. This was confirmed when the end of December and January 850 hPa temperature anomaly periods were used to generate anomaly analyses instead of daily conditions in October. The majority of the spatial domain contained positive anomalies except in the central US where the cold anomaly from the event was located. A difference between the composites and October 2020 was the warm anomalies that developed over both coasts of the US during the October 2020 ice storm on lag day 10 were not present in any of the lag days of the composite. Overall, considering the early-season timing of the event, the upper air pattern needed to be significantly amplified to allow for the cold air outbreak (and associated cold air anomalies). This is evident in the analysis.

A critical feature observed in the October 2020 ice storm was the continuous stream of ascent at the low-levels, mid-levels, and upper-levels of the atmosphere on 26 October from 0600 UTC to 1800 UTC. A moist air mass that originated in the eastern Pacific Ocean south of Baja California Sur had consistent lift from 1000 hPa to 250 hPa. The origin of the moisture was evident from the channel of higher 700 hPa water vapor anomalies indicative of an atmospheric river that originated in the tropical Pacific Ocean. This deep layer ascent of a moist air mass was necessary for heavy precipitation that occurred during this time frame evident by the radar reflectivity shown in Figure 18. In the end, and because of the persistent water vapor transport, all ingredients necessary for an ice storm were present at the same time: positive moisture anomalies originating in the tropical Pacific Ocean, a cold, low- to mid-level air mass, and abundant sources of lift (Fig. 19). This generally agrees with the research of Mullens et al. (2016) that examined high-impact ice storms in the SGP. All of these features appeared 10 days before to the day of event onset.

Because many of the features critical to this event were evident in excess of 10 days of the actual ice storm, additional analyses were completed to identify possible features in the S2S time frame that may be relevant. During October 2020, SST anomalies were influencing the upper air pattern before event onset. Higher heights (positive streamfunction) were collocated with warmer SSTs east of Japan and off the East Coast of the US. This phenomenon was also present off the West Coast of the US and British Columbia which later developed into the Alaskan Ridge seen on lag day 10. The trough in central Canada was blocked by areas of higher heights off both coasts of the US also influenced by the SSTs. Anomalously warmer SSTs that develop east of Asia and off both coasts of the US could be correlated to an upper air pattern (Alaskan Ridge and trough in central Canada) that is conducive to polar air transport and possibly winter weather.

In addition, the Alaskan Ridge and downstream trough upper air pattern could be a critical predictability signal of 2 meter cold anomalies that extend from the Arctic to the central US resulting in ice storms that impact Oklahoma. In the 2020 case, the Alaskan Ridge and trough over central Canada and the US persisted from lag day 14 to lag day 1 while a cold air anomaly over western and central Canada and the US was also present from lag day 14 to lag day 1. The relationship between mid-tropospheric geopotential heights and near-surface temperature will not guarantee an ice storm will occur every time an Alaskan Ridge and downstream trough are present because precipitation type varies on spatial and temporal scales much smaller than the synoptic scale presented in this study. However, cold surface anomalies are a necessary and critical ingredient for ice storms.

A potential limitation of this study was that only used one reanalysis dataset was utilized (ERA-5). Although the ERA-5 dataset is well-respected in the scientific community, including

more datasets such as the NCEP North American Regional Reanalysis (NARR) dataset could increase the robustness of this study. Another limiting factor is the number of past ice storm cases used to generate a climatological analysis and to compare to the October 2020 ice storm. To also increase robustness, more cases could be included and some that date back earlier than 1996.

Finally, the topics analyzed in this study could be expanded in future work. For example, the climatological analyses should be expanded and include more ice storm cases before 1996 and beyond the spatial domain of Oklahoma to the SGP and eventually the contiguous US to quantify the variability of processes in different regions. Additionally, the predictability at S2S scales should be explored further. While this study only examined 500 hPa geopotential height anomalies and predictability corresponding to 2 meter temperature anomalies, other predictability signals could be examined including SST anomalies to quantify varying spatial fields such as precipitation accumulation or precipitation type. Lastly, an area that could be examined and was not overly discussed in this study, is stratosphere-troposphere interactions as related to ice storms in Oklahoma. The standardized polar cap zonal wind anomalies from day -24 to day 5 with respect to event onset (day 0) of the October 2020 ice storm were plotted in Figure 20 and revealed that between day -10 and day -7 the lower stratosphere (50 hPa to 100 hPa) experienced weakening due to wave breaking or wave reflection (Millin et al. 2022; Matthias and Kretschmer 2020). The next steps would be to investigate exactly what process caused the stratospheric weakening in October 2020 and apply that workflow to past ice storm cases as well. The goal would be to use stratosphere-troposphere interactions as a mechanism for ice storm prediction in the SGP on the S2S timescale.

5. Conclusion

Ice storms are high-impact events that produce catastrophic impacts across space and time. The October 2020 event was no different and the impacts were heightened because it is the earliest ice storm in the last 40 years. The synoptic evolution of this ice storm was very similar to past ice storm events with the most notable features being the mid-tropospheric Alaskan Ridge and downstream trough and the cold anomaly over central Canada and the US. The geopotential height pattern was caused by higher SST anomalies seen up to two months before event onset. Although the features themselves were similar, the difference was the magnitude of these anomalies in October 2020 needed to be higher than most of the past ice storm cases to create an amplified mid- and upper-tropospheric pattern early in the winter season. October 2020 had a significantly higher lag day 1 700 hPa specific humidity maximum than the 12 past ice storm cases which allowed for abundant moisture in the atmosphere. What made this ice storm especially unique was the continuous stream of ascent of deep-tropospheric moisture necessary for an excessive precipitation event. Finally, predictability in the Alaskan Ridge and downstream trough was shown up to two weeks before event onset. This study provided an in-depth event analysis of the October 2020 ice storm while also comparing this event to past ice storm events. Ice storms are and will continue to be high-impact events that are extremely consequential. Understanding and predicting them will be of the upmost importance going forward.

References

Andrei, S., Antonescu, B., Boldeanu, M., Mărmureanu , L., Marin, C. A., Vasilescu, J., Ene, D., 2019: An Exceptional Case of Freezing Rain in Bucharest (Romania). *Atmosphere*, **10**(11): 673.

Bendel, W. B. and D. Paton, 1981: A Review of the Effect of Ice Storms on the Power Industry. *Journal of Applied Meteorology and Climatology,* **20**(12): 1445-1449.

Bowman, K. P., and C. R. Homeyer, 2017: GridRad–Three-Dimensional Gridded NEXRAD WSR-88D Radar Data, version 3.1. National Center for Atmospheric Research, Computational and Information Systems Laboratory.

Call, D. A., 2009: An Assessment of National Weather Service Warning Procedures for Ice Storms. *Weather and Forecasting*, **24**(1): 104-120.

Call, D. A., 2010: Changes in Ice Storm Impacts over Time: 1886–2000. *Weather, Climate, and Society*, **2**(1): 23-35.

Cassou, C., 2008: Intraseasonal interaction between the Madden–Julian Oscillation and the North Atlantic Oscillation. *Nature*, **455**(7212): 523-527.

Changnon, S. A., 2003: Characteristics of Ice Storms in the United States. *Journal of Applied Meteorology*, **42**(5): 630-639.

Changnon, S. A. and T. R. Karl, 2003: Temporal and Spatial Variations of Freezing Rain in the Contiguous United States: 1948–2000. *Journal of Applied Meteorology*, **42**(9): 1302-1315.

Cortinas Jr., J. V., Bernstein, B. C., Robbins, Walter Strapp, J., 2004: An Analysis of Freezing Rain, Freezing Drizzle, and Ice Pellets across the United States and Canada: 1976–90. *Weather and Forecasting*, **19**(2): 377-390.

Degelia, S. K., Christian, J. I., Basara, J. B., Mitchell, T. J., Gardner, D. F., Jackson, S. E., Ragland, J. C., Mahan, H. R., 2016: An overview of ice storms and their impact in the United States. *International Journal of Climatology*, **36**(8): 2811-2822.

Dupigny-Giroux, L. A., 2000: Impacts and consequences of the ice storm of 1998 for the North American north-east. *Weather*, **55**(1): 7-15.

Grout, T., Basara, J., Balasundaram, B., Kong, Z., and Bukkapatnam, S. T. S., 2012: Significant Winter Weather Events and Associated Socioeconomic Impacts (Federal Aid Expenditures) across Oklahoma: 2000–10. *Weather, Climate, and Society*, **4**(1): 48-58.

Hauer, R., 1993: ICE STORM DAMAGE TO URBAN TREES. *Journal of Arboriculture*, **19**: 187-194.

Hersbach, H., and Coauthors, 2020: The ERA5 global reanalysis. *Quart. J. Roy. Meteor. Soc.*, **146**, 1999–2049.

Lamb, P. J. and R. A. Peppler, 1987: North Atlantic Oscillation: Concept and an Application. *Bulletin of the American Meteorological Society*, **68**(10): 1218-1225.

Matthias, V. and M. Kretschmer, 2020: The Influence of Stratospheric Wave Reflection on North American Cold Spells. *Monthly Weather Review*, **148**(4): 1675-1690.

May, Ryan M. and Arms, Sean C. and Marsh, Patrick and Bruning, Eric and Leeman, John R. and Goebbert, Kevin and Thielen, Jonathan E. and Bruick, Zachary S. and Camron, M. Drew., 2022: Metpy: A Python Package for Meteorological Data. *Unidata*.

Millin, O. T., Furtado, J. C., and Basara, J. B., 2022: Characteristics, Evolution, and Formation of Cold Air Outbreaks in the Great Plains of the United States. *Journal of Climate*, **35**(14): 4585-4602.

Mullens, E. D., Leslie, L. M., Lamb, P. J., 2016: Synoptic Pattern Analysis and Climatology of Ice and Snowstorms in the Southern Great Plains, 1993–2011. *Weather and Forecasting*, **31**(4): 1109-1136.

Namias, J., 1938: Thunderstorm Forecasting With The Aid of Isentropic Charts. *Bulletin of the American Meteorological Society*, **19**(1): 1-14.

National Weather Service, 2001: December 25-26, 2000: Ice Storm Strikes the ArkLaTex. Shreveport LA.

National Weather Service, 2008: The December 8-11, 2007 Ice Storm in Oklahoma. Norman OK.

Oklahoma Mesonet, 2002: January 28-30, 2002: Oklahoma Ice Storm.

Oklahoma Mesonet, 2016: Oklahoma's Historic 2015 Weather Ends With A Bang.

Ramos da Silva, R., Bohrer, G., Werth, D., Otte, M. J., Avissar, R., 2006: Sensitivity of Ice Storms in the Southeastern United States to Atlantic SST—Insights from a Case Study of the December 2002 Storm. *Monthly Weather Review*, **134**(5): 1454-1464.

Rauber, R. M., Olthoff, L. S., Ramamurthy, M. K., Miller, D., and Kunkel, K. E., 2001: A Synoptic Weather Pattern and Sounding-Based Climatology of Freezing Precipitation in the United States East of the Rocky Mountains. *Journal of Applied Meteorology*, **40**(10): 1724-1747.

Ressler, G. M., Milrad, S. M., Atallah, E. H., and Gyakum, J. R., 2012: Synoptic-Scale Analysis of Freezing Rain Events in Montreal, Quebec, Canada. *Weather and Forecasting*, **27**(2): 362-378.

Robbins, C. C. and J. V. Cortinas, 2002: Local and Synoptic Environments Associated with Freezing Rain in the Contiguous United States. *Weather and Forecasting*, **17**(1): 47-65.

Roebber, P. J. and J. R. Gyakum, 2003: Orographic Influences on the Mesoscale Structure of the 1998 Ice Storm. *Monthly Weather Review*, **131**(1): 27-50.

Ropelewski, C. F. and M. S. Halpert, 1986: North American Precipitation and Temperature Patterns Associated with the El Niño/Southern Oscillation (ENSO). *Monthly Weather Review* **114**(12): 2352-2362.

Schwartz, C. and C. I. Garfinkel, 2017: Relative roles of the MJO and stratospheric variability in North Atlantic and European winter climate. *Journal of Geophysical Research Atmospheres*, **122**(8): 4184-4201.

Wheeler, M. C. and H. H. Hendon, 2004: An All-Season Real-Time Multivariate MJO Index: Development of an Index for Monitoring and Prediction. *Monthly Weather Review*, **132**(8): 1917-1932.

Zarnani, A., Musilek, P., Shi, X., Ke, X., He, H., and Greiner, R., 2012: Learning to predict ice accretion on electric power lines. *Engineering Applications of Artificial Intelligence*, **25**(3): 609-617.

Appendix

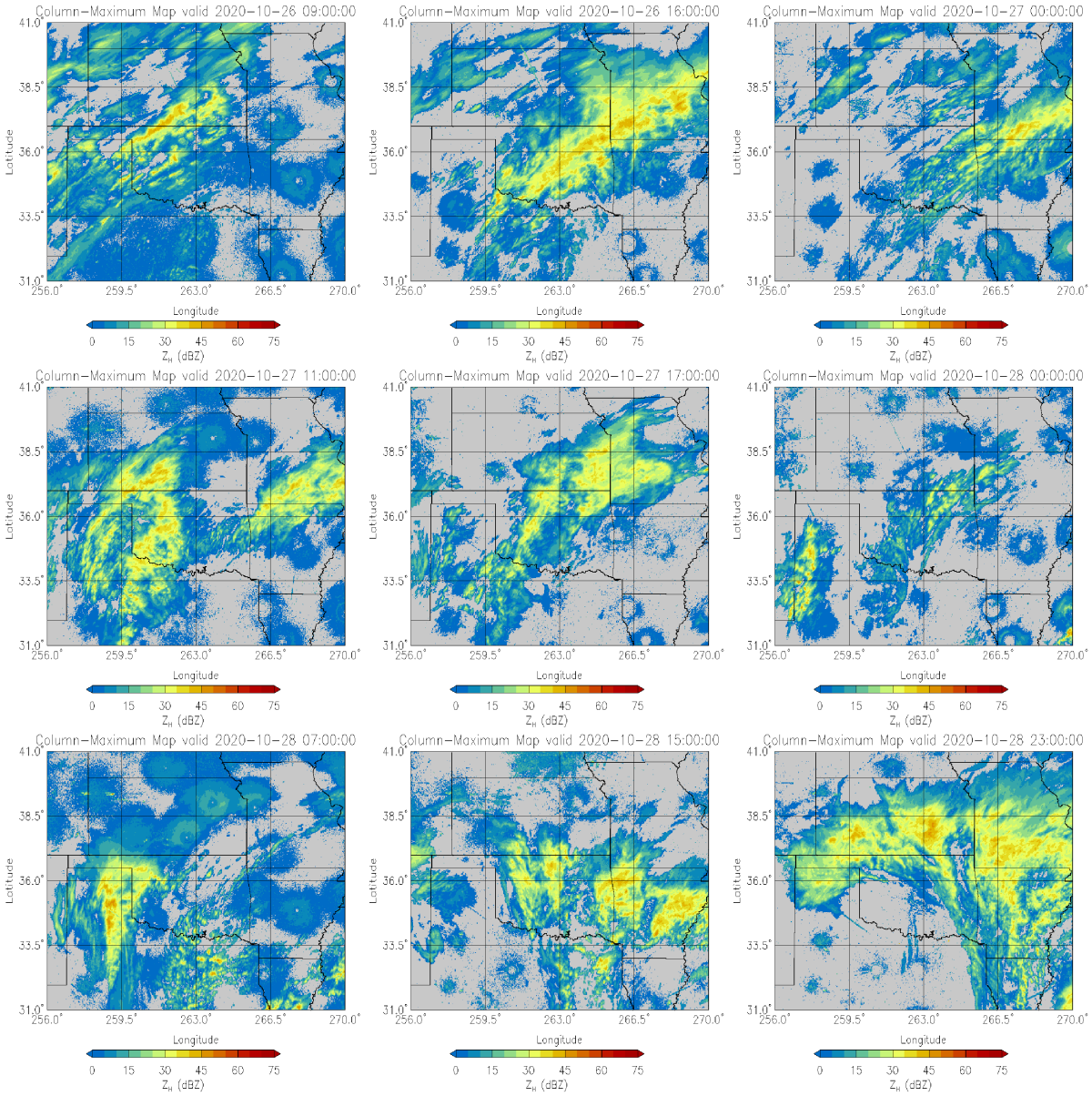

Figure 1: Multi-panel plot of radar reflectivity from the timestamps of 26 October 0900 UTC and 1600 UTC, 27 October 0000 UTC, 1100 UTC, and 1700 UTC, and 28 October 0000 UTC, 0700 UTC, 1500 UTC, and 2300 UTC.

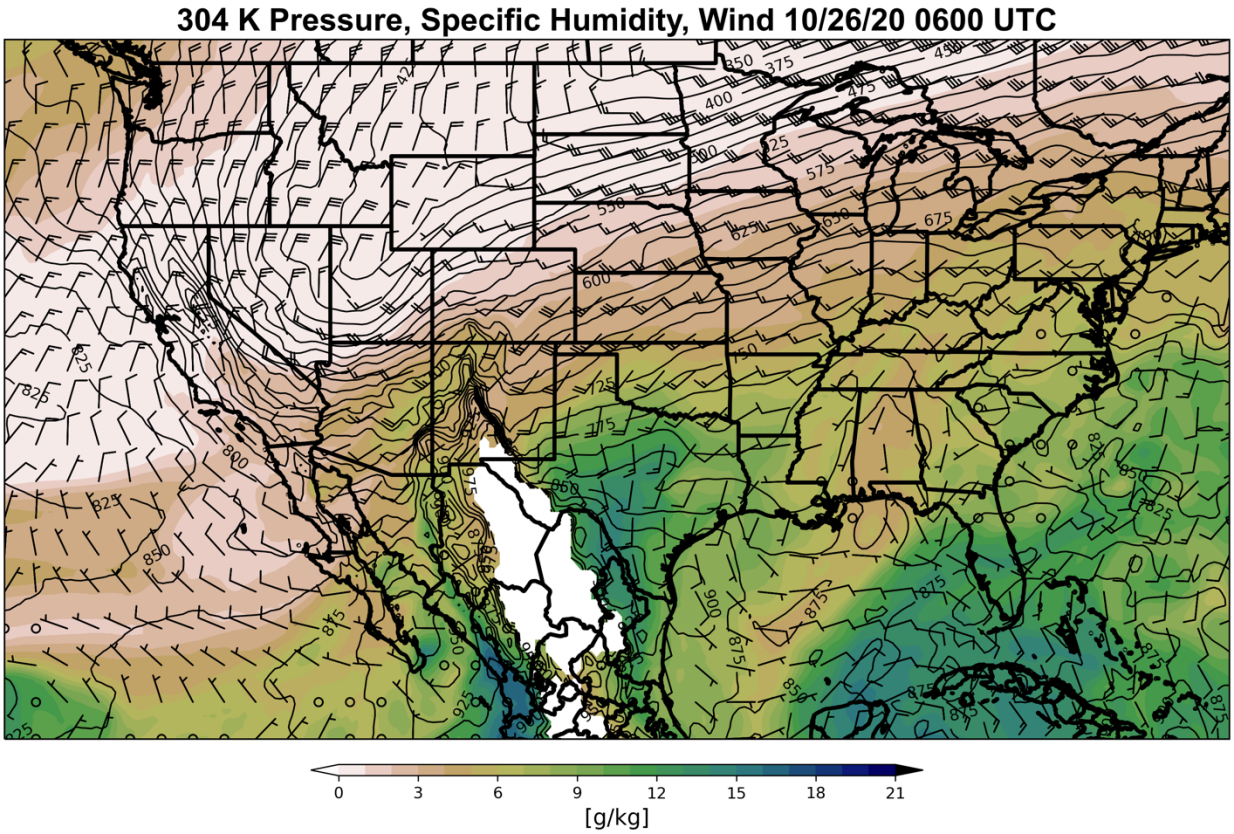

Figure 2: Isentropic ascent analyzed on the 304 K isentrope level for 26 October 0600 UTC. The black contours are isobars, the shading is specific humidity (g/kg), and wind barbs are also included.

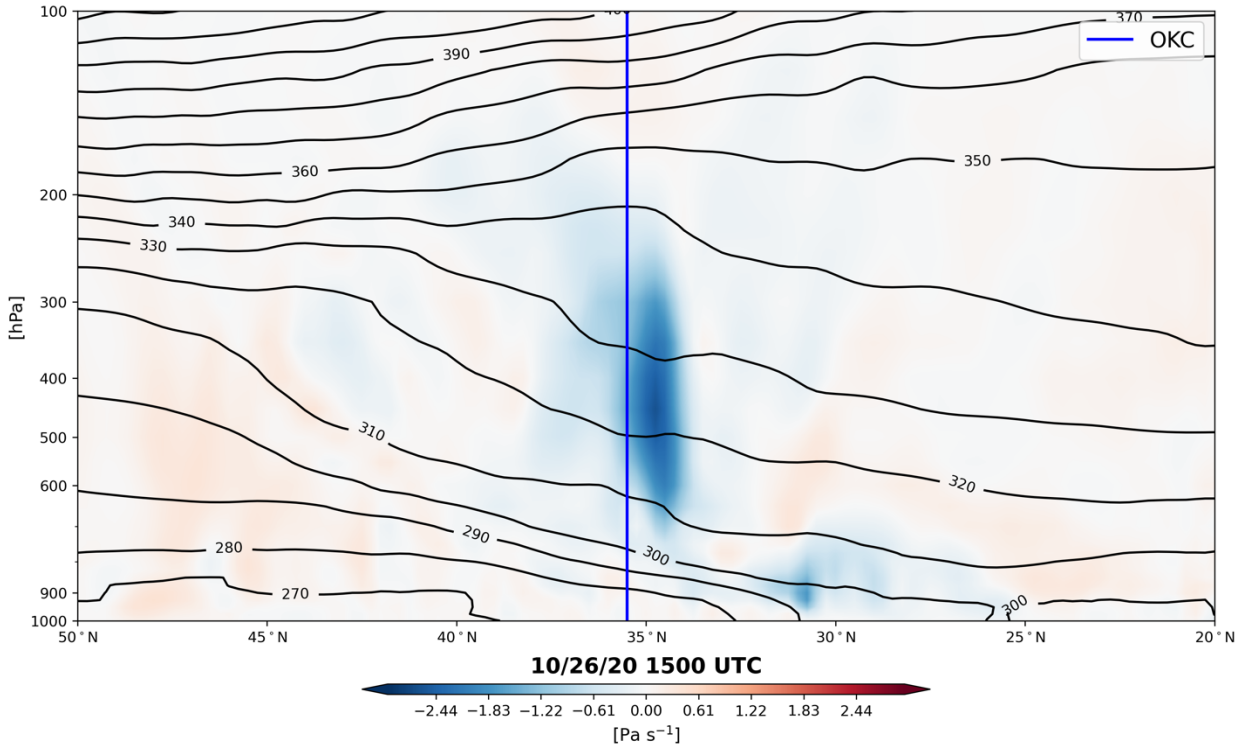

Figure 3: Vertical cross section of potential temperature (black contours) and vertical motion (shading) for 26 October 1500 UTC.

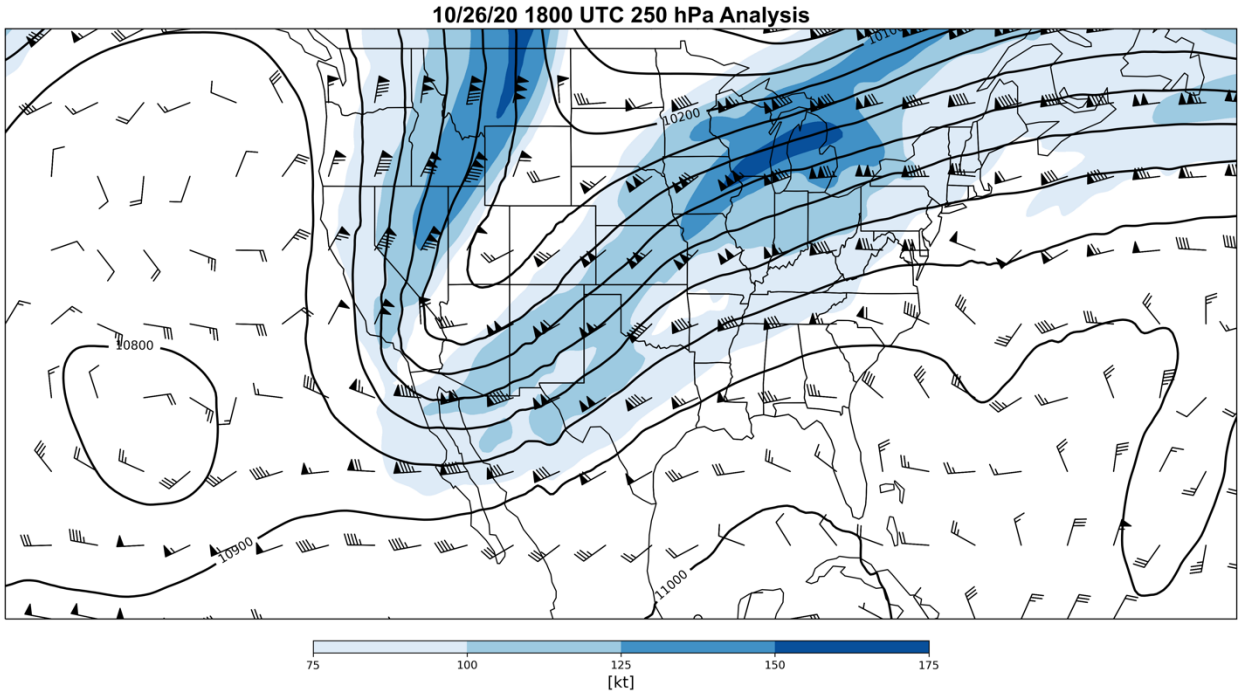

Figure 4: 250 hPa analysis for 26 October 1800 UTC. The black contours are lines of constant geopotential height. Wind barbs are included with shading starting at 75 knots and every 25 knots after.

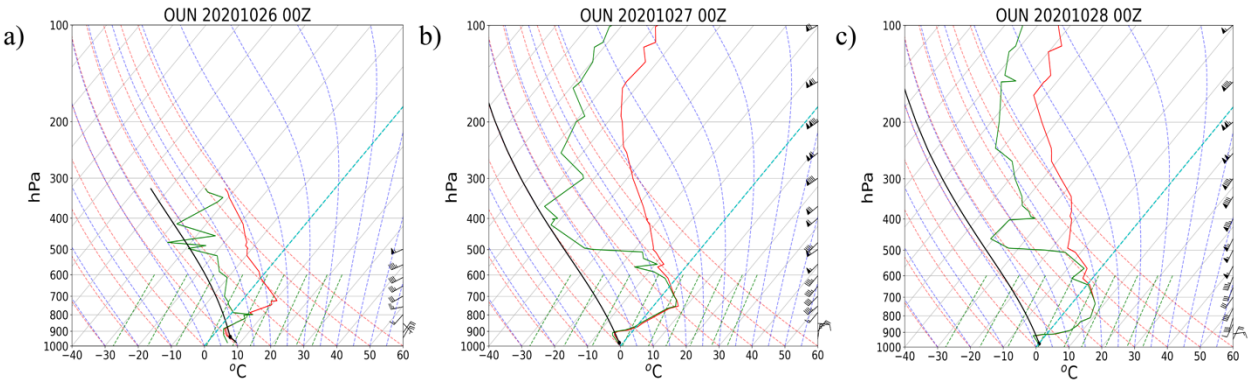

Figure 5: Soundings from NWS Norman on 26 October 0000 UTC, 27 October 0000 UTC, and 28 October 0000 UTC.

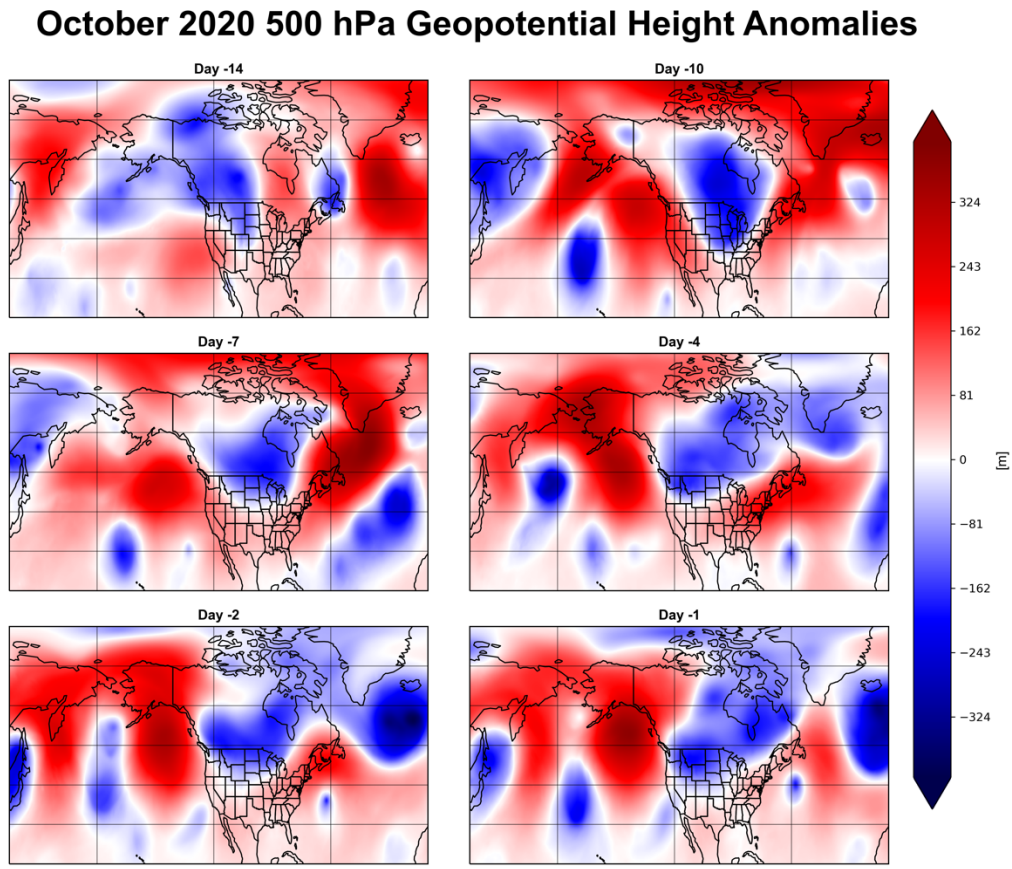

Figure 6: 500 hPa geopotential height anomalies calculated using a daily climatology for lag days 14, 10, 7, 4, 2, and 1 before the onset of the October 2020 ice storm.

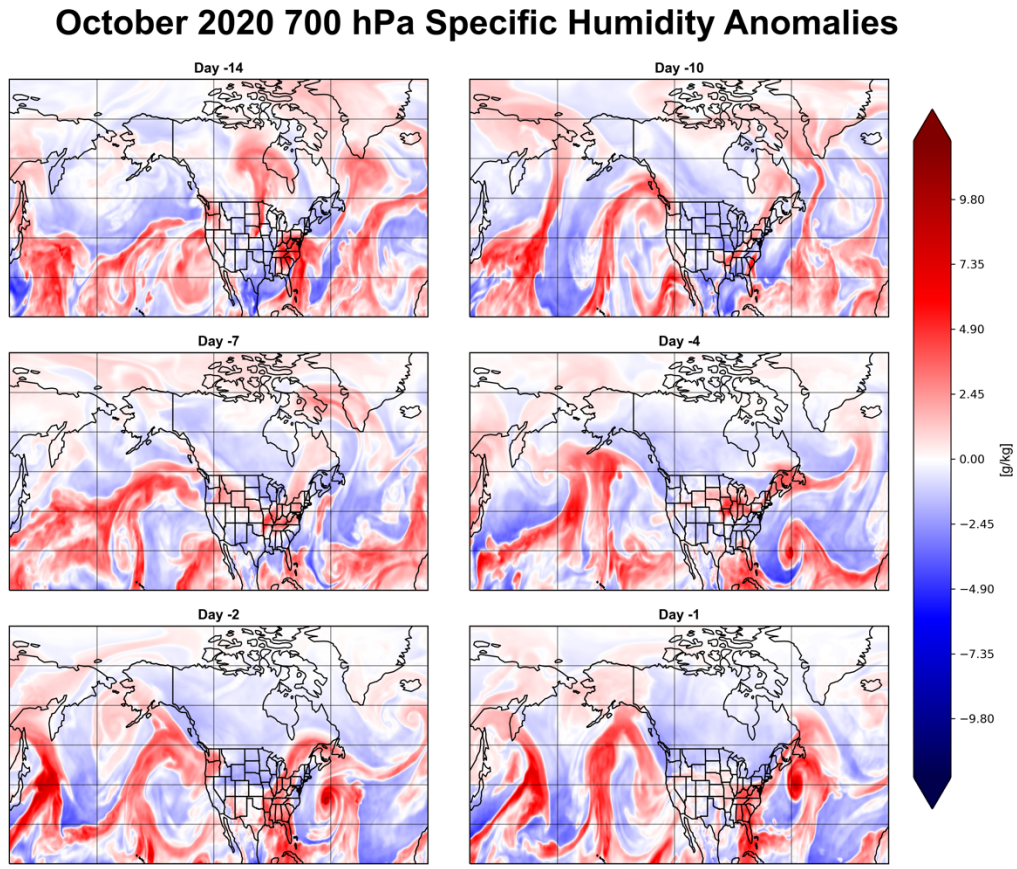

Figure 7: 700 hPa specific humidity anomalies calculated using a daily climatology for lag days 14, 10, 7, 4, 2, and 1 before the onset of the October 2020 ice storm.

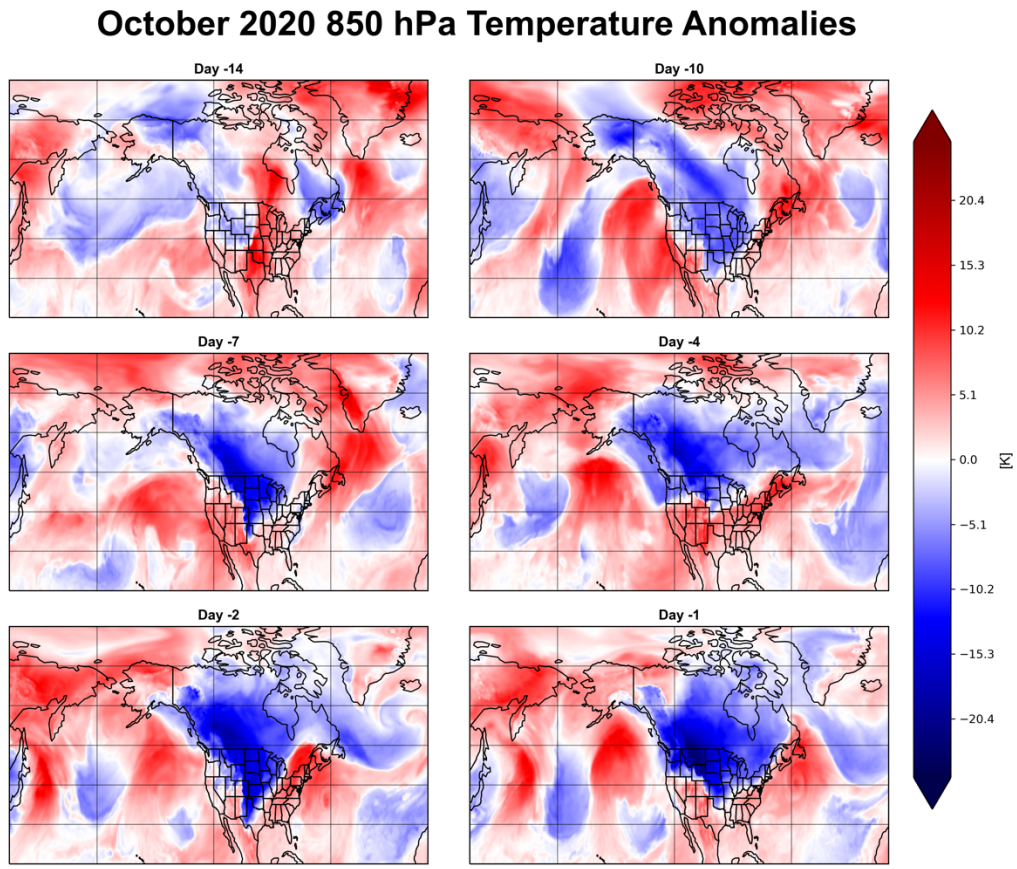

Figure 8: 850 hPa temperature anomalies calculated using a daily climatology for lag days 14, 10, 7, 4, 2, and 1 before the onset of the October 2020 ice storm.

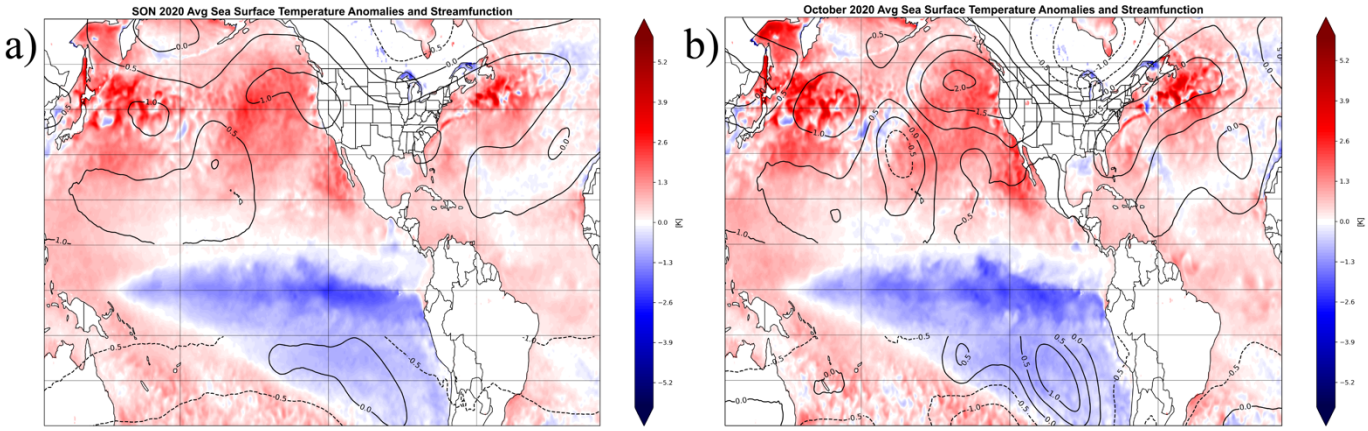

Figure 9: The shading is averaged SST anomalies over (a) SON 2020 and (b) October 2020 and the black contours are 250 hPa QG streamfunction anomalies (10^6 m^2s^{-1}).

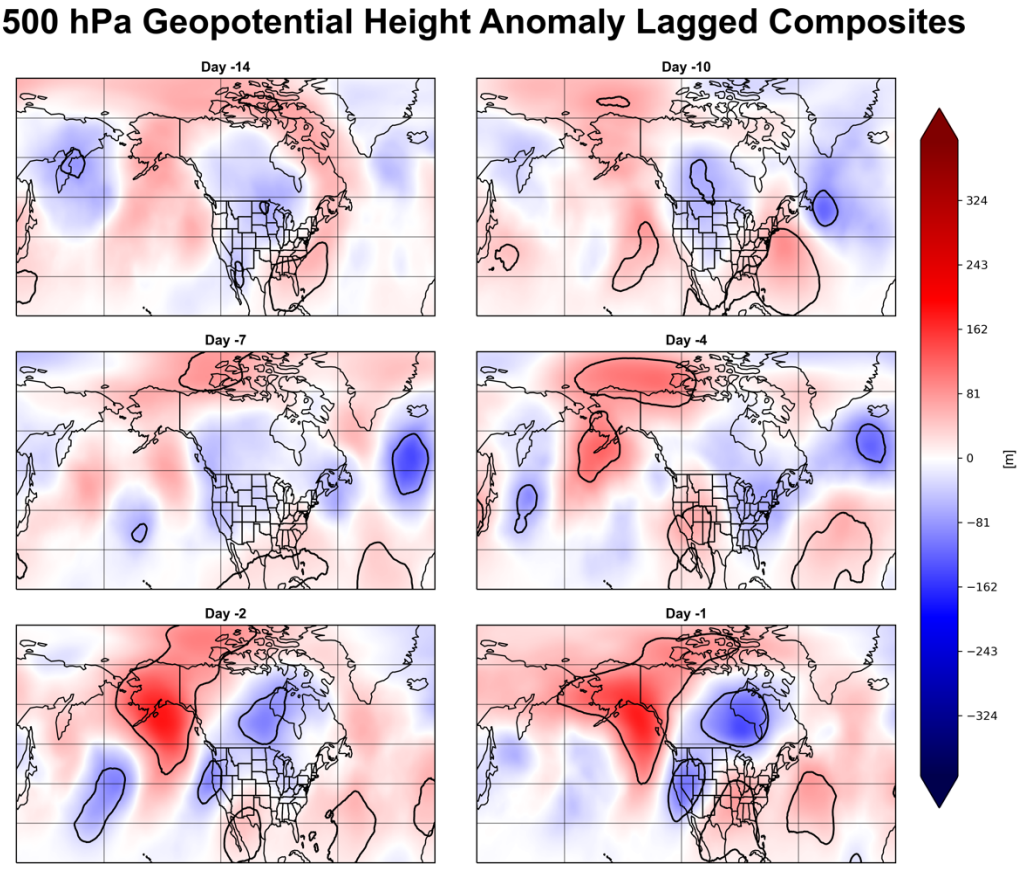

Figure 10: Time-lagged composites of 500 hPa geopotential height anomalies (shading) calculated using a daily climatology for the 12 past ice storms for lag days 14, 10, 7, 4, 2, and 1 before event onset. The black contours represent statistical significance at the 95th percentile using 5000-iteration bootstrapping without replacement.

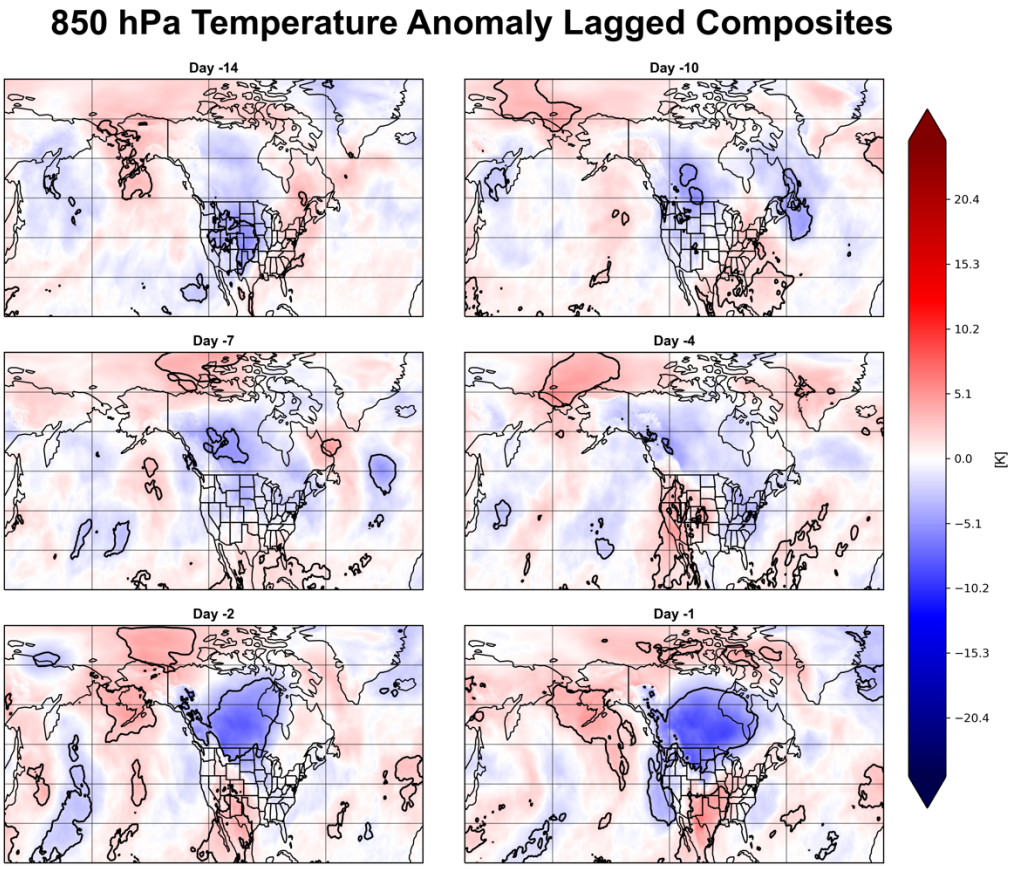

Figure 11: Time-lagged composites of 850 hPa temperature anomalies (shading) calculated using a daily climatology for the 12 past ice storms for lag days 14, 10, 7, 4, 2, and 1 before event onset. The black contours represent statistical significance at the 95th percentile using 5000-iteration bootstrapping without replacement.

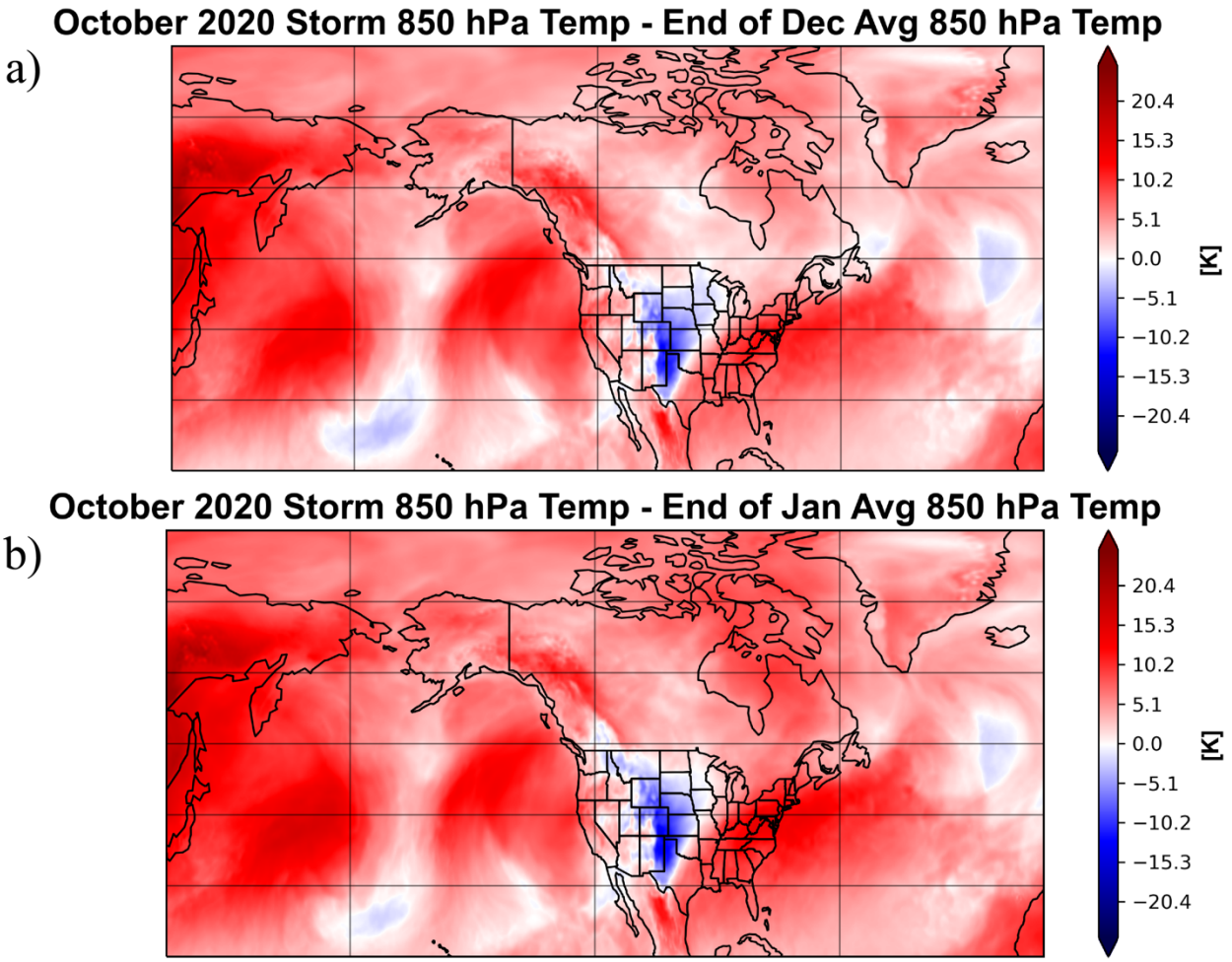

Figure 12: 850 hPa temperature anomalies of the October 2020 ice storm (26 to 28 averaged) using the (a) end of December (15 to 31) and (b) end of January (15 to 31) climatology.

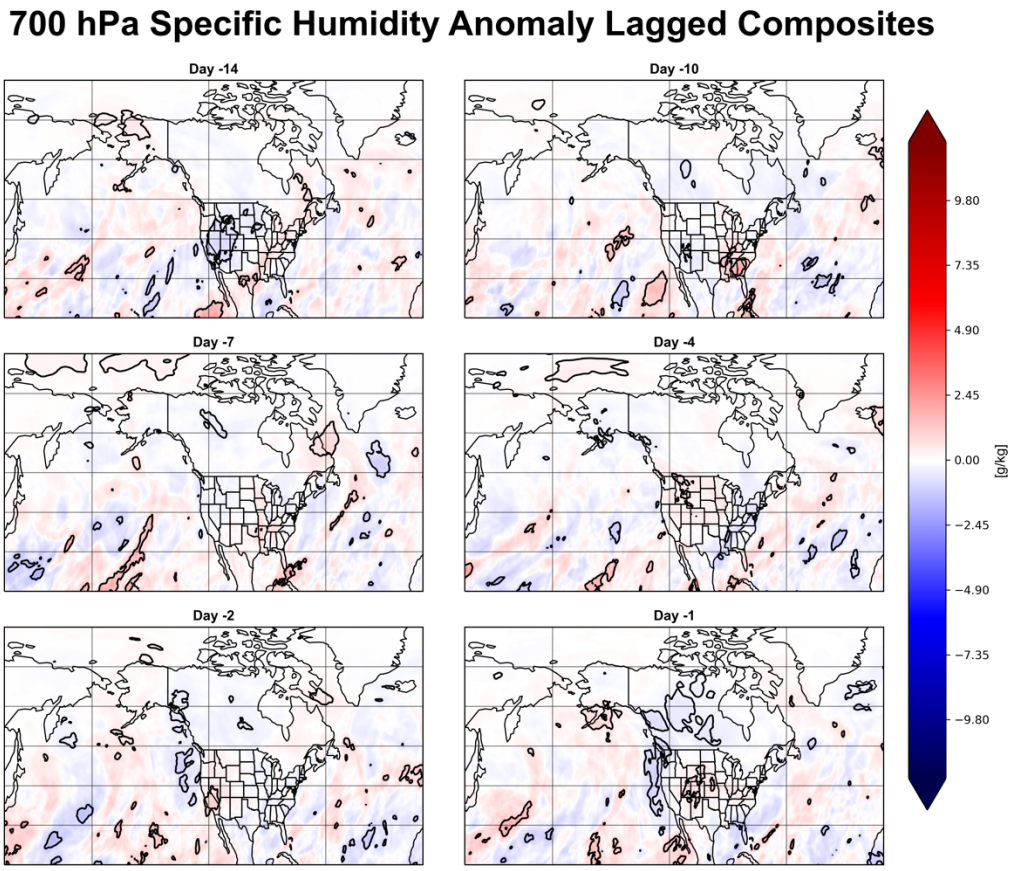

Figure 13: Time-lagged composites of 700 hPa specific humidity anomalies (shading) calculated using a daily climatology for the 12 past ice storms for lag days 14, 10, 7, 4, 2, and 1 before event onset. The black contours represent statistical significance at the 95th percentile using 5000-iteration bootstrapping without replacement.

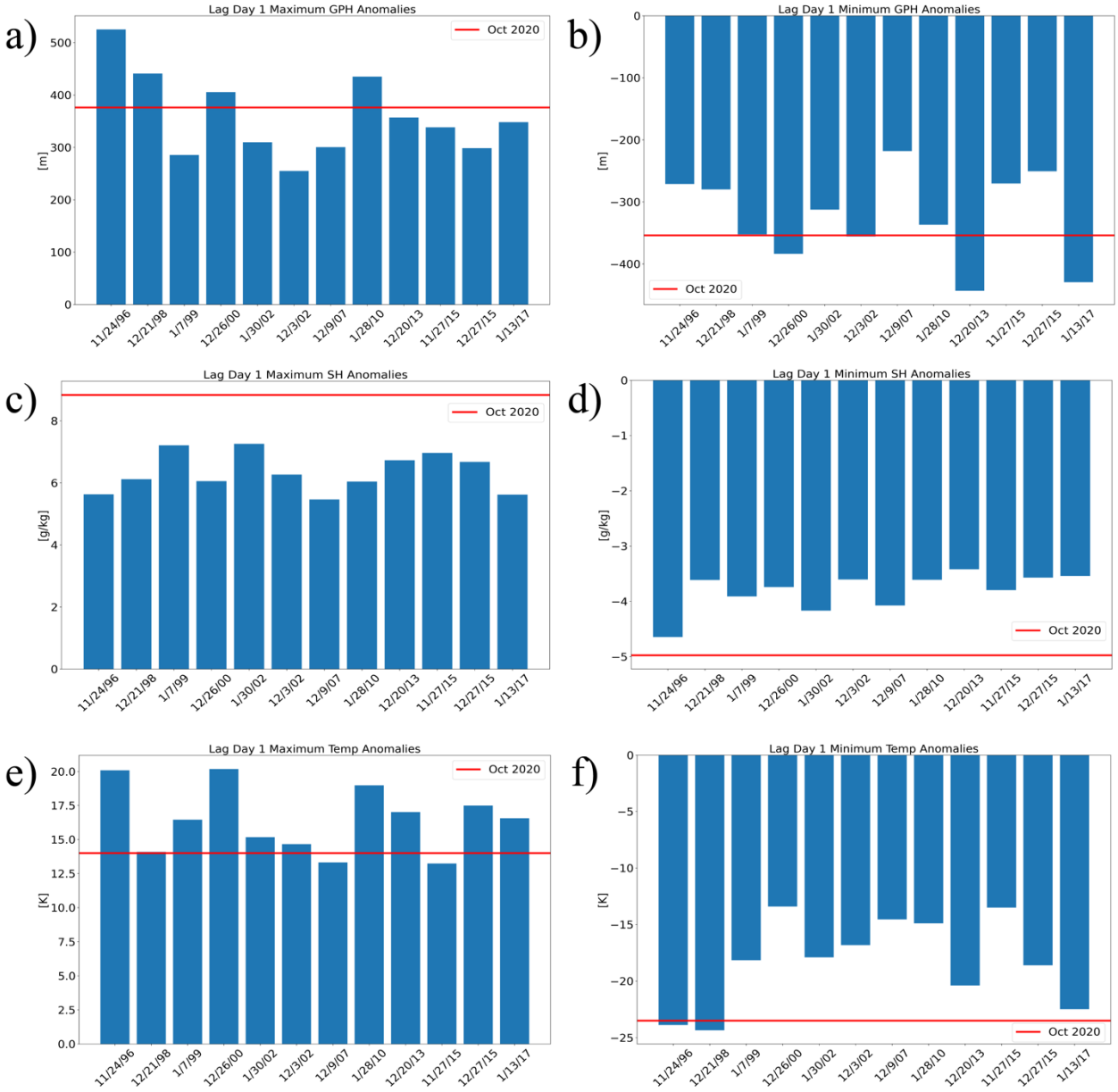

Figure 14: Bar charts of the 12 past ice storms (blue bars) and October 2020 (red line) for panel (a) maximum 500 hPa geopotential height anomaly, (b) minimum 500 hPa geopotential height anomaly, (c) maximum 700 hPa specific humidity anomaly, (d) minimum 700 hPa specific humidity anomaly, (e) maximum 850 hPa temperature anomaly, and (f) minimum 850 hPa temperature anomaly for lag day 1.

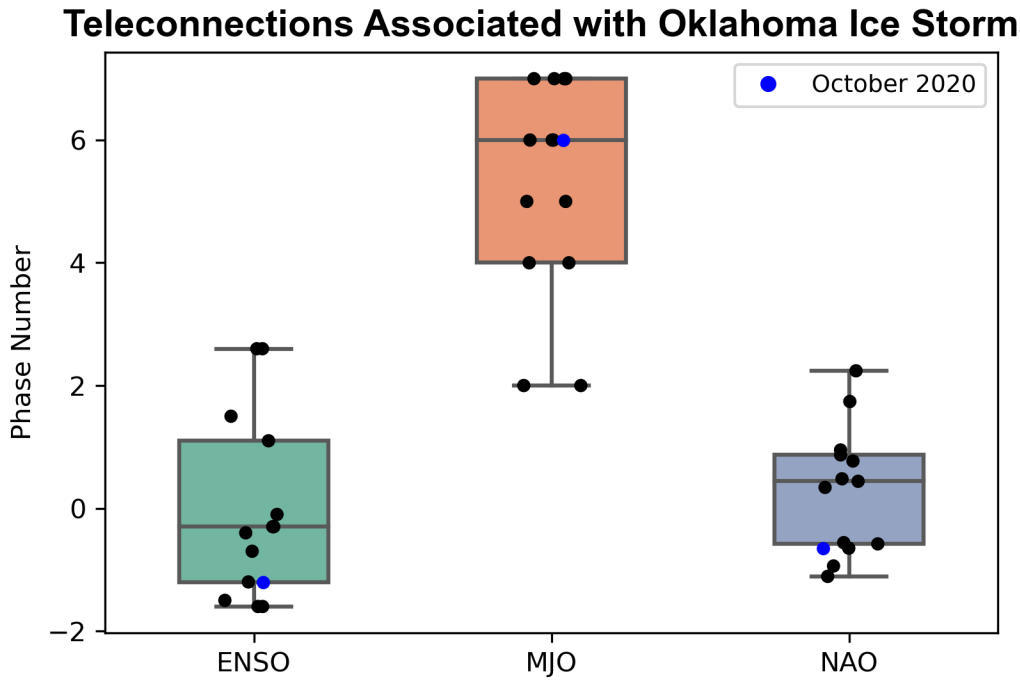

Figure 15: Box and whisker plot of ENSO, MJO, and NAO phases of each of the 12 past ice storm events (black dots) and October 2020 ice storm (blue dot).

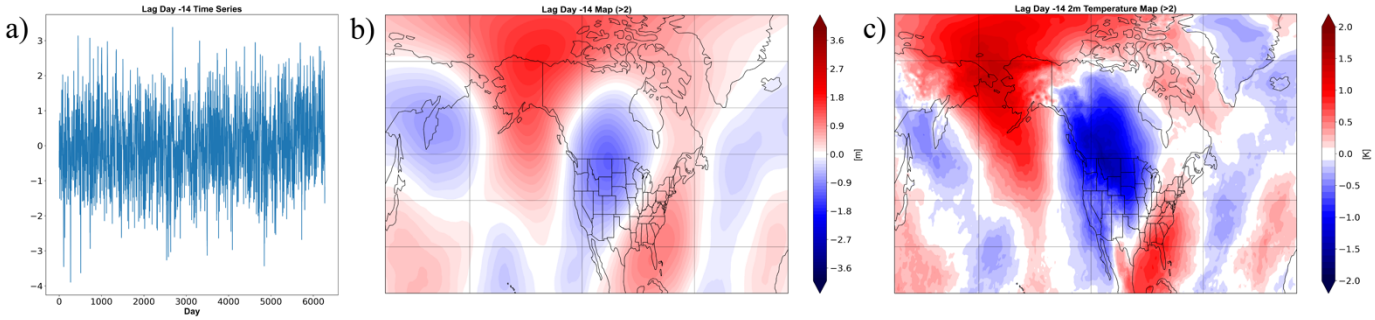

Figure 16: Panel (a) is a time series of indices measuring how well each day in the dataset (SONDJ 1979 - 2020) measures the lag day 14 500 hPa geopotential height anomalies composite. The next two panels are composites of (b) 500 hPa geopotential height anomalies and (c) 2 meter temperature anomalies of all the days whose index exceeded two.

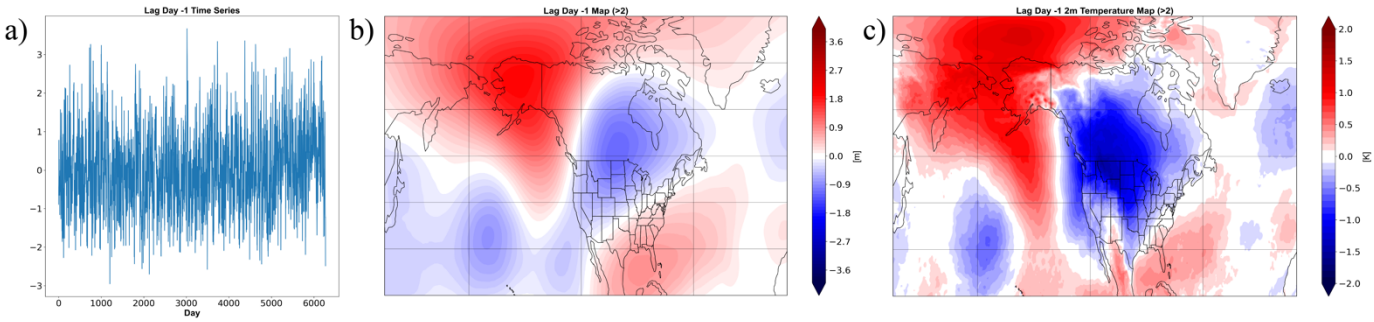

Figure 17: Panel (a) is a time series of indices measuring how well each day in the dataset (SONDJ 1979 - 2020) measures the lag day 1 500 hPa geopotential height anomalies composite. The next two panels are composites of (b) 500 hPa geopotential height anomalies and (c) 2 meter temperature anomalies of all the days whose index exceeded two.

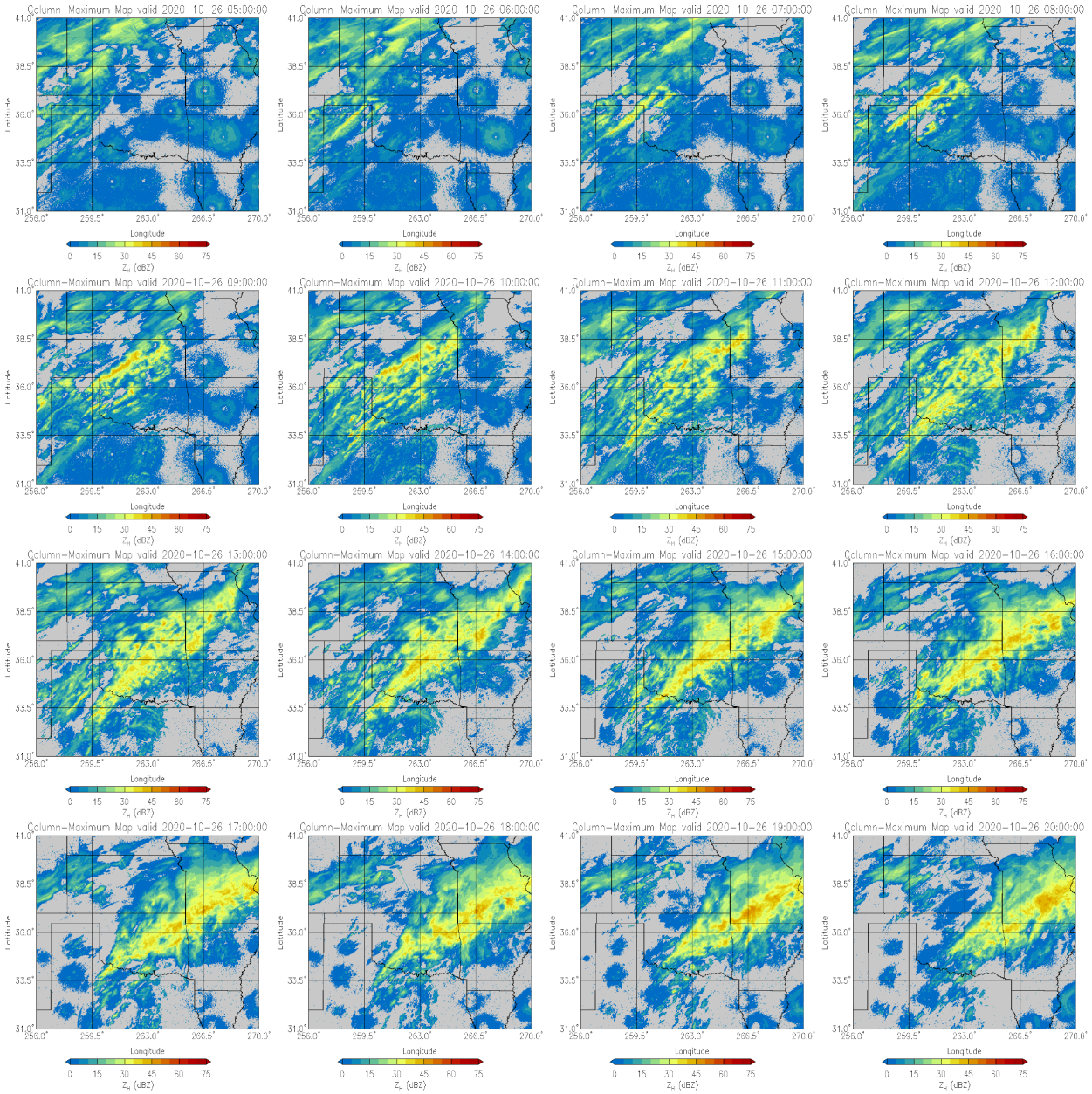

Figure 18: Multi-panel plot of hourly radar reflectivity on 26 October from 0500 UTC to 2000 UTC.

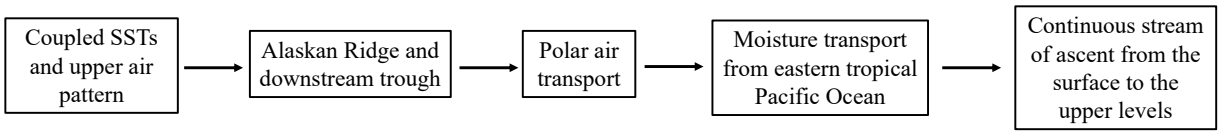

Figure 19: A flowchart of the important features leading to the October 2020 ice storm.

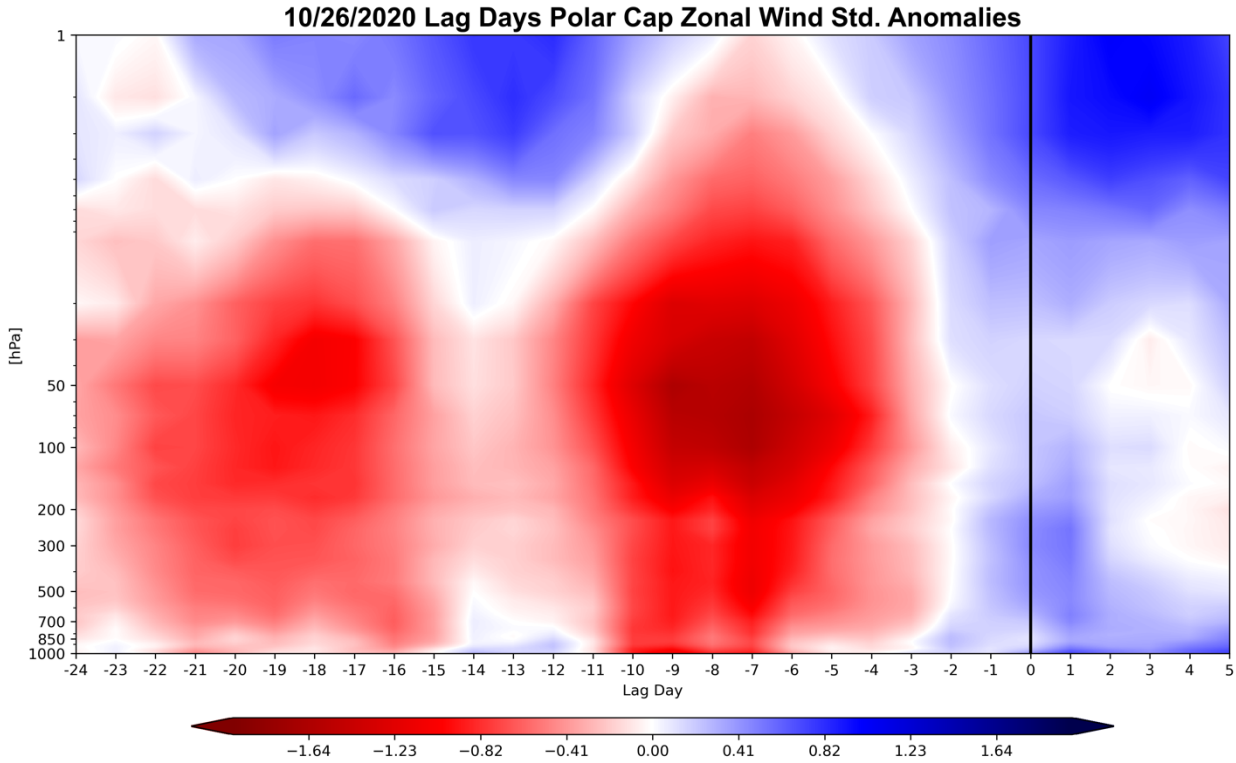

Figure 20: Polar cap zonal wind standardized anomalies for day -24 through 5 with respect to event onset (day 0) of the October 2020 ice storm.